Indication of exchange interaction induced spin splitting in unoccupied electronic states of the high-T_C ferromagnet $(Cr_{0.35}Sb_{0.65})_2Te_3$

C. W. Chuang [1,2] Y. Nakata,[1] K. Hori,[1] S. Gupta,[3,4,5,*] F. M. F. de Groot,[6] A. Fujimori,[7,8,9] T. P. T. Nguyen,[10] K. Yamauchi,[10,11] I. Rajput,[12] A. Lakhani,[12] F.-H. Chang,[2] H.-J. Lin,[2] C.-T. Chen,[2] F. Matsukura,[3,4,5] S. Souma [4,13] T. Takahashi,[1,4,13] T. Sato,[1,4,13,14] and A. Chainani [2]

[1]*Department of Physics, Graduate School of Science, Tohoku University, Sendai 980-8578, Japan*
[2]*National Synchrotron Radiation Research Center, Hsinchu 30076, Taiwan, Republic of China*
[3]*Center for Innovative Integrated Electronic Systems, Tohoku University, Sendai 980-0845, Japan*
[4]*Advanced Institute for Materials Research (WPI-AIMR), Tohoku University, Sendai 980-8577, Japan*
[5]*Laboratory for Nanoelectronics and Spintronics, Research Institute of Electrical Communication, Tohoku University, Sendai 980-8577, Japan*
[6]*Inorganic Chemistry and Catalysis, Utrecht University, Universiteitsweg 99, 3584 CG Utrecht, The Netherlands*
[7]*Department of Physics, The University of Tokyo, 7-3-1 Hongo, Bunkyo-ku, Tokyo 113-0033, Japan*
[8]*Center for Quantum Technology, and Department of Physics, National Tsing Hua University, Hsinchu 30013, Taiwan, Republic of China*
[9]*Condensed Matter Physics Group, National Synchrotron Radiation Research Center, Hsinchu 30076, Taiwan, Republic of China*
[10]*Institute of Scientific and Industrial Research, Osaka University, Osaka 567-0047, Japan*
[11]*Center for the Promotion of Interdisciplinary Education and Research, Kyoto University, Kyoto 606-8501, Japan*
[12]*UGC-DAE Consortium for Scientific Research, University Campus, Khandwa Road, Indore-452001, India*
[13]*Center for Spintronics Research Network, Tohoku University, Sendai 980-8577, Japan*
[14]*Center for Science and Innovative in Spintronics, Tohoku University, Sendai 980-8577, Japan*

(Received 29 May 2022; revised 28 January 2024; accepted 23 April 2024; published 10 May 2024)

We study the high Curie temperature ferromagnet $(Cr_{0.35}Sb_{0.65})_2Te_3$ ($T_C = 192$ K), using T-dependent x-ray absorption spectroscopy (XAS), x-ray magnetic circular dichroism (XMCD), and angle-resolved photoemission spectroscopy (ARPES). The T-dependent (25–220 K) XAS-XMCD evolution of Cr $3d$ and Te $5p$ unoccupied site- and orbital-projected states shows a systematic modification, which we interpret as due to spin-splitting below T_C. The T-dependent XMCD intensity and leading-edge spin-sensitive shifts $\gamma_{expt}(T)$ follow bulk magnetization. ARPES measurements with $h\nu = 78$ eV show a metallic state with Sb $5p$ band dispersions at and near Fermi level (E_F), consistent with bulk band-structure calculations for $(Cr_{0.33}Sb_{0.67})_2Te_3$. However, surface-sensitive ARPES with $h\nu = 8.4$ eV above and below T_C show linear band dispersions just below E_F, suggesting a remnant of Dirac-type dispersions. Assuming the linear dispersion survives above E_F, it implies a topologically trivial ferromagnet as the estimated Dirac point energy lies above the largest γ_{expt} ($T = 25$ K). The Cr $3d$ XAS-XMCD spectra can be simulated by charge transfer multiplet cluster model calculations with an exchange field H_{ex} which quantitatively reproduces the experimental XMCD. At $T = 25$ K, the required exchange field H_{ex} of ~48 T corresponds to a Zeeman energy $\zeta = 2.8$ meV $< T_C = 192$ K (= 16.5 meV) $\ll \gamma_{expt} \sim 140$ meV. The results indicate the role of Cr $3d$ exchange interactions in causing spin-sensitive shifts in Cr $3d$ states, and inducing comparable spin-sensitive shifts via hybridization in Te $5p$ states of $(Cr_{0.35}Sb_{0.65})_2Te_3$.

DOI: 10.1103/PhysRevB.109.195134

I. INTRODUCTION

Magnetic doping in a topological insulator (TI) with Dirac-type linear topological surface state (TSS) dispersions breaks time-reversal symmetry and can lead to ferromagnetic (FM) ordering [1–5]. In a three-dimensional (3D) TI, the onset of FM order leads to the formation of a T-dependent magnetic gap at the Dirac point (DP) [4]. The combination of a FM insulator and a topologically nontrivial SS, which is necessary for realizing the quantum anomalous Hall effect (QAHE) with dissipationless quantized edge-state transport without an external magnetic field, also requires that the Fermi level (E_F) lies in the magnetic gap [5–8].

The observation of a genuine magnetic gap in magnetic TIs has challenged researchers over the past 10 years. While early angle-resolved photoemission spectroscopy (ARPES) work showed a gap of ~50 meV in TSSs of $(Bi_{0.84}Fe_{0.16})_2Se_{3.7}$ with a $T_C = 170$ K [9], studies on magnetic Mn-doped Bi_2Se_3 reported larger gaps of ~50–200 meV [10,11] which were later shown to be unrelated to FM ordering [12]. Scanning tunneling spectroscopy showed gaps of 20–100 meV in Cr-doped TIs at low-T [13], but later studies showed a gap of ~75 meV above $T_C \sim 50$ K and ruled out a magnetic origin of the gap [14].

*Present address: Department of Physics, School of Engineering and Applied Sciences, Bennett University, Greater Noida 201310, India.

Recent ARPES measurements on $Bi_2Te_3/MnBi_2Te_4$, a natural heterostructure material with a $T_C \sim 10$ K, showed a T-dependent magnetic gap of ~ 90 meV at $T = 1$ K [15], while another study reported a magnetic gap of ~ 28 meV at $T = 7$ K [16]. Both studies measured the magnetic gap at the DPs derived from occupied Bi-Te p-character TSSs. Similarly, a DP magnetic gap with a high-T_C of ~ 50 K in $MnSb_2Te_4$ was also reported in Sb-Te p-character occupied TSSs [17]. For Bi_2Se_3, Bi_2Te_3, and related materials, spin-resolved ARPES has characterized the spin-polarized Dirac cones, and shown that DPs lie between E_F and ~ 300 meV below E_F [18]. On the other hand, for Sb_2Te_3 and related systems, the DP lies 30–300 meV above E_F as identified by pump-probe (PP)-ARPES [18]. PP-ARPES of Sb_2Te_3 showed a DP at 190 meV above E_F, which shifts to 220 meV above E_F for V-doped Sb_2Te_3 [18]. For Cr-doped Sb_2Te_3, valence-band ARPES reported shifts due to hole doping [19], but PP-ARPES has not been reported. In a recent ARPES study on epitaxial films of $(Cr_xSb_{1-x})_2Te_3$, $x = 0.0$, 0.05, 0.15, and 0.35 grown on GaAs(111) substrates, we have reported on the evolution of band dispersions and Fermi surfaces [20]. The results showed a systematic hole doping induced shift, and assuming the DP survives above E_F, its energy is estimated to vary from ~ 30 meV above E_F for $x = 0.0$ to ~ 240 meV above E_F for $x = 0.35$.

It is important to note that single crystals of $(V/Cr_xSb_{1-x})_2Te_3$ were studied as spintronic materials before the discovery of the TI properties of Sb_2Te_3 [21] and showed T_C's up to ~ 20 K for $x = 0.03$–0.1. A pioneering molecular-beam-epitaxy study [22] showed that T_C's of $\sim$100–190 K could be achieved for $x = 0.15$–0.3. X-ray absorption spectroscopy (XAS) and x-ray magnetic circular dichroism (XMCD) studies of $(Cr_{0.16}Sb_{0.84})_2Te_3$ with $T_C \sim 87$ K showed a Cr spin moment, $m_{\text{spin}} \approx 3\mu_B$ [23]. Using a cluster model analysis with d^3 and $d^4\underline{L}^1$ basis states, where $\underline{L}^1$ is a ligand hole state, the authors concluded that the ground state can be described using a positive charge-transfer (CT) energy Δ [23]. More recently, XAS and XMCD studies on $Cr_{0.1}(Bi_{0.1}Sb_{0.9})_{1.9}Te_3$ with a $T_C \sim 20$ K concluded a negative Δ using cluster model calculations with a larger basis set of $d^{n+p}\underline{L}^p$ states ($n = 3$ and $p = 0$–3) [24,25]. While T-dependent XMCD intensity up to 30 K was reported, the T-dependent XAS and XMCD spectral changes were not reported.

Thus, a detailed study of T-dependent XAS-XMCD spectral changes has not been reported yet for any magnetically doped TI. It is also not yet known whether the Dirac-type linear bands and the DP expected to lie above E_F survive in the highest $T_C \sim 190$ K case of $(Cr_{0.35}Sb_{0.65})_2Te_3$, and whether it shows a topological magnetic gap. The answer to this question is necessary to decide whether $(Cr_{0.35}Sb_{0.65})_2Te_3$ is a topological ferromagnet or a topologically trivial ferromagnet. Since it is established from earlier studies that the Te M-edge derived XAS-XMCD in Cr-doped Sb_2Te_3 forms a well-separated prepeak below the leading edge of the Cr L-edge XAS [23–25], it is possible to probe the T-dependent spectral changes in the unoccupied Cr $3d$ and Te $5p$ states, i.e., in the root source of the magnetism as well as the unoccupied Te $5p$ states. In particular, since dopant states are expected to be localized and not show T-dependence, how they actually participate and cause long-range T-dependent magnetic order in any doped TI is also an open question. While it is well-known that the magnetic gap in a TI can arise from an exchange coupling of the dopant spins with topological surface states [26], the relation of T_C and spin-splitting energy scale with the internal exchange field (H_{ex}) has not been reported for any TI doped with magnetic ions.

In this work, we have carried out a T-dependent XAS-XMCD and ARPES study of $(Cr_{0.35}Sb_{0.65})_2Te_3$ epitaxial films which exhibit a $T_C \sim 192$ K. Since excitonic effects occur in XAS spectra, based on the formal definition of charge-transfer multiplet calculations, the as-such calculated XAS spectrum of final-state excitons correlates with the Cr site- and orbital symmetry-projected spin-sensitive unoccupied electronic states, and a calculated spin shift will translate into a shift in the XMCD multiplet states [27,28]. Bulk-sensitive ARPES shows Sb $5p$ band dispersions cross E_F, indicating a metallic ground state consistent with electrical resistivity and bulk band-structure calculations. The bulk band-structure calculations show a small gap of ~ 150 meV lying just above E_F at and near the Γ-point. While surface-sensitive ARPES shows remnant Dirac-type linear bands in $(Cr_{0.35}Sb_{0.65})_2Te_3$, the DP cannot be confirmed by ARPES as it is estimated to lie ~ 250 meV above E_F. The Cr L-edge and Te M-edge XAS with an applied field shows a T-dependent XMCD and spin-sensitive shifts in the Cr $3d$ and Te $5p$ leading edges below T_C. The T-dependent XMCD signal intensity and the spin-sensitive shifts $\gamma_{\text{expt}}(T)$ follow the bulk magnetization. However, since the largest γ_{expt} ($T = 25$ K) ~ 140 meV is less than the estimated DP at ~ 250 meV above E_F, it implies $(Cr_{0.35}Sb_{0.65})_2Te_3$ is a topologically trivial FM. The T-dependent XMCD in the Cr $3d$ states can be simulated by an exchange field. The results indicate that the spin-sensitive shifts in Cr $3d$ originate from exchange interactions, and they induce comparable spin-sensitive shifts in Te $5p$ states.

II. METHODS

A. Sample preparation and characterization

Epitaxial films of $(Cr_{0.35}Sb_{0.65})_2Te_3$ were grown on semi-insulating GaAs(111)B substrates by molecular beam epitaxy (MBE), as reported earlier [29]. The sample thickness was about 60 nm as measured by cross-sectional scanning electron microscopy. $(Cr_{0.35}Sb_{0.65})_2Te_3$ crystallizes in the tetradymite structure like the parent Sb_2Te_3, as shown in Fig. 1. The θ-2θ x-ray diffraction (XRD) pattern of $(Cr_{0.35}Sb_{0.65})_2Te_3$ was measured using Cu $K\alpha$ radiation as shown in Fig. 2(a). The XRD pattern showed a pure single phase with (00l) peaks of the tetradymite structure. Magnetization measurements with an applied field of 2 mT normal to the surface (parallel to c-axis) were carried out using a physical property measurement system (PPMS, Quantum Design, USA) and the results showed a FM onset Curie temperature $T_C = 192$ K, as shown in Fig. 2(b). The single-crystal Sb_2Te_3 reference sample was made by a self-flux method, and its characterization was reported earlier [30].

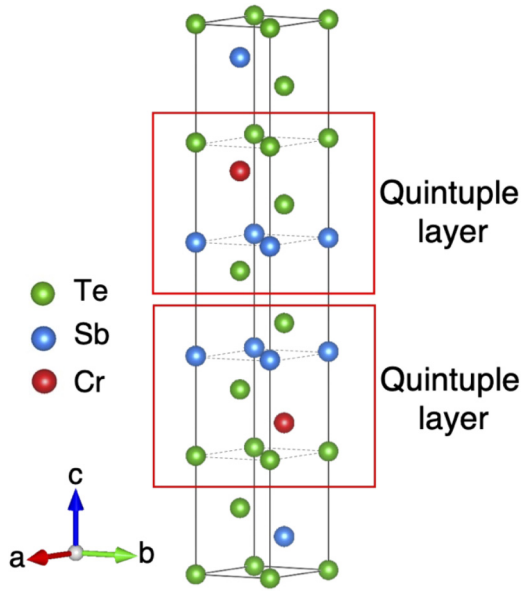

FIG. 1. The crystal structure of $(Cr_{0.33}Sb_{0.67})_2Te_3$, showing two Cr substituted sites (red) in the parent Sb_2Te_3 tetradymite structure, corresponding to $x = 0.33$, which was used for the LDA + U calculations.

B. XAS-XMCD and ARPES experimental details

XAS and XMCD measurements were carried out at Dragon Beamline (BL 11A) of the Taiwan Light Source. The total electron yield method was used to measure XAS and XMCD across the Te $M_{4,5}$-edges ($3d$-$5p$) and Cr $L_{2,3}$-edges ($2p$-$3d$) with circularly polarized light and an applied magnetic field of ± 1 T. The magnetic field was applied normal to the sample surface (parallel to the c-axis), which is favorable for observation of the magnetic gap at a DP. If the magnetic field is near parallel to the surface, then the DP gets shifted in two-dimensional (2D) momentum space in the direction perpendicular to the field and suppresses the gap opening [26]. The x-rays were incident at an angle of 30° off the c-axis. The total energy resolution at the Cr L-edge was better than 0.2 eV for the XAS and XMCD spectra, as set by the slit size. The incident photon energy has an accuracy of ± 10 meV at the Cr L-edge. The Te M-edge spectrum of Sb_2Te_3 was measured at $T = 300$ K. All spectra reported here were carefully calibrated using the Cr L-edge XAS of Cr_2O_3, which was measured simultaneously upstream of the sample measurement chamber. For XAS and XMCD measurements, the epitaxial films as well as the parent Sb_2Te_3 single crystal were cleaved *in situ* in the main chamber in an ultrahigh vacuum (UHV) of better than 8×10^{-10} mbar. For XAS-XMCD and ARPES measurements, a Te capping layer of ∼50 nm was deposited on top of the film after sample growth, and then it was extracted from the MBE chamber. An aluminum post was mounted on top of the Te capping layer, the sample was loaded into the XAS-XMCD/ARPES chamber, and then cleaved in UHV to obtain a clean surface, following earlier work [23,24,31]. The samples showed clean shiny surfaces after cleaving, with spectral shapes consistent with reports for lower Cr-doping samples [23,24]. The surface cleanliness was checked by O K-edge measurements, and it showed negligible intensity during the course of the measurements. Further, the Cr L-edge spectra of epitaxial films are quite different from the reference Cr_2O_3, which was measured simultaneously. The samples were cooled using a liquid He flow type cryostat, and the measurements were carried out for selected temperatures down to $T = 25$ K.

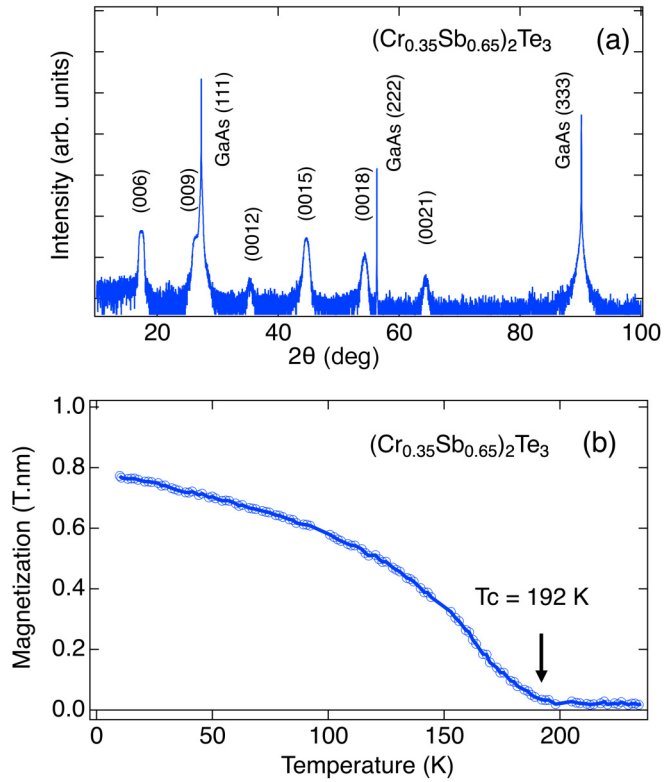

FIG. 2. (a) θ-2θ x-ray diffraction pattern of $(Cr_{0.35}Sb_{0.65})_2Te_3$ showing a pure single phase with (00l) peaks. (b) T-dependent magnetization of $(Cr_{0.35}Sb_{0.65})_2Te_3$, showing a ferromagnetic onset $T_C = 192$ K.

ARPES measurements were carried out using a spectrometer equipped with a Scienta-Omicron DA30 analyzer at beamline BL-28A of Photon Factory, KEK. Circularly polarized light with a photon energy ($h\nu$) of 78 eV was used to measure band dispersions. It is known that $h\nu = 78$ eV probes the bulk-origin valence-band dispersions [19], and this was also confirmed by us [20]. ARPES measurements were also carried out for $(Cr_{0.35}Sb_{0.65})_2Te_3$ with an MBS-A1 electron analyzer equipped with a high-intensity Xe plasma discharge lamp at Tohoku University [32]. The samples were cleaved in the main chamber at an ultrahigh vacuum of 1.5×10^{-10} mbar. We used one of the Xe I lines ($h\nu = 8.437$ eV) to measure the surface-sensitive bands. The energy and momentum resolutions for the ARPES measurements were set to 15 meV and 0.01 Å^{-1}, respectively. For $h\nu = 8.437$ eV, the sample temperature was set to $T = 20$ and 210 K to probe below and above T_C, respectively.

III. RESULTS AND DISCUSSION

Figures 3(a)–3(d) shows the T-dependent (25–220 K) Cr L-edge and Te M-edge experimental XAS and XMCD

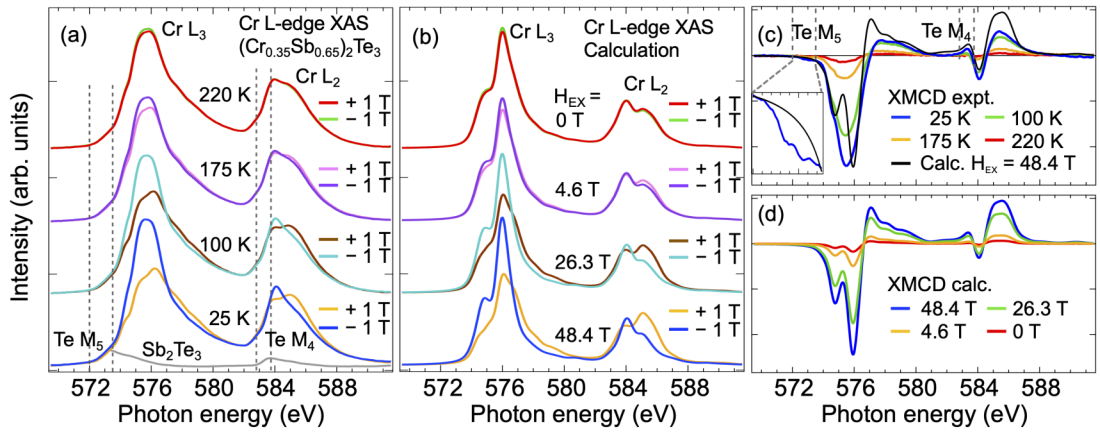

FIG. 3. (a) The T-dependent (25–220 K) Cr L-edge and Te M-edge range XAS spectra from *in-situ* cleaved surfaces of $(Cr_{0.35}Sb_{0.65})_2Te_3$ with an applied magnetic field of ± 1 T. The Te M-edge range XAS spectra from *in situ* cleaved Sb_2Te_3 is also shown, and the gray vertical dashed lines mark the Te M_5 and Te M_4 leading edge ranges. (b) The corresponding calculated Cr L-edge XAS spectra obtained with an applied magnetic field of ± 1 T and exchange field H_{ex} as listed in the figure. (c) The T-dependent (25–220 K) Cr L-edge and Te M-edge experimental XMCD intensity. The Te M_5-edge XMCD signal is seen as a small prepeak marked by vertical gray lines (expanded in the inset), at photon energies below the L_3-edge XMCD, but the Te M_4-edge XMCD overlaps the Cr L_2-edge XMCD. The calculated XMCD spectrum for $T = 25$ K is also shown as a black line. (d) The corresponding calculated Cr L-edge XMCD spectra for different values of exchange field H_{ex} quantitatively reproduce the experimental XMCD intensity at the Cr L_3 main peak.

spectra from *in situ* cleaved surfaces of $(Cr_{0.35}Sb_{0.65})_2Te_3$ with an applied magnetic field of ± 1 T, together with corresponding calculated spectra. A polynomial background was subtracted from the raw XAS spectra as shown in the Appendix, Fig. 9. The spectra were then plotted after normalizing the XAS spectra without an applied field at the intensity of the L_3 edge main peak for all T. It is known from low-energy electron diffraction of the parent Sb_2Te_3 [31] that cleaving results in a Te-terminated (0001) surface. The obtained spectra after cleaving are very consistent with earlier studies, which reported XAS-XMCD spectra after cleaving at a low T of 10 K (for a $T_C = 87$ K sample) [23], and at $T = 2$ K (for a $T_C = 20$ K sample) [24]. The same procedure of cleaving also provided clear ARPES spectra, as reported by us recently [20]. The XAS spectral shape and intensities change systematically on increasing T from 25 to 220 K, above $T_C = 192$ K. Using the known assignments from earlier work [23–25], the Cr L-edge XAS spectrum consists of the spin-orbit split L_3 features between ~573.5 and 580 eV and L_2 features between ~583 and 588 eV. To separate out the Te M-edge features, the XAS of single crystal Sb_2Te_3 was measured and is shown as a gray curve in Fig. 3(a). The Te M_5 leading edge is identified as lying between ~572 and ~573.5 eV photon energy [gray dashed lines in Fig. 3(a)], with an onset ~1.5 eV below the Cr L_3 leading-edge onset, as is well-established from earlier studies [23–25], while the Te M_4 edge is between ~582 and ~583 eV, overlapping with the Cr L_2-edge states. Since the Te M_5 leading edge is ~1.5 eV below the Cr L_3 edge onset, and it is known that the core-level binding energy separation is 10 eV for Te $3d$ and 9 eV for Cr $2p$ states as measured by photoemission [33], the lowest energy unoccupied states are attributed to the Te $5p$ states in the XAS-XMCD spectra. While T-dependent spectral changes are observed over the full range, the most important and subtle changes occur at the Te M_5 and Cr L_3 leading edges, and to understand them in context, we first discuss the XMCD and ARPES spectra in the following.

The T-dependent XMCD spectra were obtained as the difference between the $+1$ and -1 T XAS spectra and are shown in Fig. 3(c). The XMCD signal intensity shows a systematic decrease on increasing T from 25 to 220 K. The maximum negative XMCD signal is at $h\nu \sim 575.4$ eV due to the Cr L_3 edge main peak. The Cr L_3 main peak XMCD signal is preceded by a small negative prepeak appearing between $h\nu \sim 572$ and 573.5 eV due to the Te M_5 edge XMCD signal. At higher photon energies, the main XMCD signal is followed by a positive XMCD between $h\nu \sim 577$ and 580 eV. The L_2 edge XMCD shows a small dip at $h\nu \sim 584$ eV and a positive XMCD between $h\nu \sim 585$ and 587.5 eV. It is noted that a small XMCD signal is observed at $T = 220$ K in the paramagnetic phase, above $T_C = 192$ K, as the applied magnetic field aligns the magnetic moments in the paramagnetic phase [34].

To understand the Cr L-edge XAS-XMCD spectral features of $(Cr_{0.35}Sb_{0.65})_2Te_3$, we carried out charge-transfer multiplet cluster model calculations using the QUANTY program [35–37]. Following earlier studies [23,24], and because first-principles calculations showed that Cr atoms prefer to occupy Sb sites with the lowest formation energy [38,39], we consider a $CrTe_6$ cluster in octahedral (O_h) symmetry. The Cr dopant is considered to be trivalent, and the basis states are given by $d^{n+p}\underline{L}^p$ states ($n = 3$ and $p = 0$–3) [24]. The calculation method is described in the Appendix. The calculated spectra shown in Fig. 3(b) were obtained for an on-site Coulomb energy $U_{dd} = 4.0$ eV, core-hole potential $U_{cd} = 4.8$ eV, hybridization strengths $V_{eg} = 1.35$ eV, $V_{t_{2g}} = 0.5$ eV, crystal-field splitting $10Dq = 1.0$ eV, and CT energy $\Delta = -2.0$ eV. The obtained parameters including the negative $\Delta = -2.0$ eV are consistent with recent studies on $Cr_{0.1}(Bi_{0.1}Sb_{0.9})_{1.9}Te_3$ [24] and Cr_2Te_3 [40], which showed

a negative $\Delta = -2.0$ and -1.0 eV, respectively. The calculated spectra show deviations from experiment, particularly for the main Cr L_3 peak, which consists of two broad peaks merged together, while the calculations show two well separated peaks, and our attempts to improve the calculated spectra were not successful. This suggests limitations of the cluster model, as earlier reports also showed very similar differences between experimental and calculated XAS spectra [23–25], although the shape of the calculated XMCD spectra qualitatively reproduces the experimental spectral features. Further, the T-dependent experimental XMCD intensity at the L_3 edge main peak could be quantitatively reproduced (within an accuracy of ±1%) only by including an appropriate exchange field H_{ex} in addition to the applied experimental magnetic field. Thus we could calculate spectra for the T-dependent experimental XMCD intensity as shown in Fig. 3(d).

It is noted that the negative Δ results in the initial state being dominated by the CT states $d^4\underline{L}$ (51.77%) and $d^5\underline{L}^2$ (36.90%), with very small contribution from $3d^3$ (8.44%) and $d^6\underline{L}^3$ (2.89%) states, consistent with Tcakaev *et al.* [24] The magnetic moment was estimated from the cluster model calculations as well as a sum-rule analysis of the spectra, which give a spin magnetic moment of $\sim 3.0 \pm 0.2 \mu_B$ for $(Cr_{0.35}Sb_{0.65})_2Te_3$ with negligible orbital magnetic moment, consistent with reported values [22–24]. The results also show that the weak XMCD intensity between 572 and 573.5 eV is not due to the Cr $3d$ states but to Te $5p$ states [inset of Fig. 3(c)]. An important aspect of negative Δ is that it leads to a p-p type lowest energy excitation in CT materials like $NaCuO_2$ and $NdNiO_3$ with $U_{dd} > |\Delta|$, as the lowest unoccupied states also have ligand character [41–43]. Thus, in the present case, the lowest unoccupied states are confirmed to be Te $5p$ states. Another important piece of evidence of Te $5p$ character in the unoccupied states is the presence of Dirac-type linear bands associated with band inversion in TIs [1–3,7–9]. Hence, we measured ARPES with different photon energies to investigate bulk- and surface-sensitive band dispersions. We also carried out band-structure calculations for the composition $(Cr_{0.33}Sb_{0.67})_2Te_3$, which is close to our sample composition of $(Cr_{0.35}Sb_{0.65})_2Te_3$, in order to characterize the electronic states near E_F, as detailed below.

Band-structure calculations were carried out in the local density approximation with on-site Coulomb energy (LDA+U) using the QUANTUM ESPRESSO code. For $(Cr_{0.33}Sb_{0.67})_2Te_3$, two out of six Sb sites which correspond to the lowest formation energy [38,39] were substituted by Cr atoms, as shown in Fig. 1. LDA calculations were also carried out for the parent compound Sb_2Te_3. The lattice parameters were fixed to the experimentally known values of $a = 4.25$ Å, $c = 30.35$ Å. Figure 4(a) shows the Brillouin zone of Sb_2Te_3 with labeled high-symmetry points. Figures 4(b) and 4(c) show the calculated band dispersions of Sb_2Te_3 and $(Cr_{0.33}Sb_{0.67})_2Te_3$ along high-symmetry cuts in the Brillouin zone obtained from band-structure calculations. In Fig. 4(b), The Sb (green) and Te (purple) band dispersions of Sb_2Te_3 at and near the Γ point indicate a gap with band inversion, with the valence-band states being dominated by Sb p-states and the conduction-band states being dominated by Te p-states. In Fig. 4(d), we plot the projected Te $5p_{3/2}$ and $5p_{1/2}$ partial DOS compared with the corresponding Te M_5 and M_4 edge XAS spectra obtained from Sb_2Te_3 single crystal. The leading edges of the experimental Te M_5 and M_4 edges are aligned and normalized for intensity to the calculated PDOS, but the relative intensities for the trailing edges of the Te M_5 and M_4 edges are lower in experiment compared to the calculations. Nonetheless, the experimental spectral width and features are consistent with the calculations and confirm the Te $5p$ character states. It is noted that XAS of ligand states such as O K-edge and S L-edge have been compared with the calculated band density of states in transition metal compounds [44,45].

The calculated Sb (green) and Te (purple) band dispersions of $(Cr_{0.33}Sb_{0.67})_2Te_3$ shown in Fig. 4(c) indicate that the band inversion, which is a necessary condition to obtain TSS [1–3], survives after Cr doping at and near the Γ point, although with small relative changes in the Sb $5p$ and Te $5p$ bands compared to LDA results of Sb_2Te_3 shown in Fig. 4(b). Upon Cr substitution, the calculations show that the valence-band states have moved up towards E_F compared to Sb_2Te_3 and they cross the E_F, consistent with the effective hole doping due to Cr substitution and a metallic ground state, as seen in electrical resistivity [29]. Figure 4(e) shows the calculated band dispersions of $(Cr_{0.33}Sb_{0.67})_2Te_3$ for the high-symmetry cuts in the Brillouin zone over a wide energy range. The green and yellow bands are the projected Cr $3d_{5/2}$ and $3d_{3/2}$ bands, and the symbol size reflects the relative DOS. Figure 4(f) shows the corresponding momentum integrated total DOS (black line) and the projected $3d_{5/2}$ and $3d_{3/2}$ PDOS. The Sb-Te p-character bands dominate at and near E_F while the main Cr $3d$ PDOS consisting of t_{2g} up-spin occupied states and t_{2g} down-spin unoccupied states are obtained between 2 and 4 eV below and above E_F, respectively. It is noted that the weak Cr $3d$ PDOS feature just above E_F in Fig. 4(f) originates from states lying between the M- and K-points as seen in Fig. 4(e). The band assignments are quite similar to that of another van der Waals layered FM CrI_3 [46].

Figure 4(g) shows the ARPES intensity map of $(Cr_{0.35}Sb_{0.65})_2Te_3$ obtained for the Γ-M cut using $h\nu = 78$ eV to probe the bulk bands. A broad M-shaped spectral feature is seen in the ARPES intensity map. The band-structure results of $(Cr_{0.33}Sb_{0.67})_2Te_3$ for Γ-M ($k_z = 0$) and A–L ($k_z = \pi$) cuts are overlaid in Fig. 4(g). The calculated bands show a good match with the data and indicate that dominantly Sb-Te $5p$ states constitute the spectral intensity at E_F and within ±2 eV of E_F. The occurrence of band inversion indicates that the linear surface-state bands would be of mainly Sb $5p$ orbitals below the DP and mainly of Te $5p$ orbitals above the DP, if the DP exists. Further, at and near the Γ point, the dominantly Sb-Te $5p$ states show a gap of ∼150 meV just above E_F in the bulk states, as seen in Fig. 4(g). The presence of this gap can facilitate TSS with linear Dirac-type band dispersions to be retained for Cr content $x = 0.35$. We have also confirmed that this gap above E_F is not obtained in LDA calculations for $U = 0$, as the main Cr $3d$ unoccupied states lie just at and above E_F for $U = 0$, consistent with earlier work [25,47].

Next, in Figs. 5(a) and 5(b), we show the raw ARPES intensity maps of *in situ* cleaved surfaces of $(Cr_{0.35}Sb_{0.65})_2Te_3$ films measured at $T = 210$ and 20 K using $h\nu = 8.4$ eV from a xenon lamp [32]. We found that $h\nu = 8.4$ eV is suitable to trace the dispersion of SS by avoiding overlap with the k_z-dispersive bulk valence bands [20]. The dashed lines trace

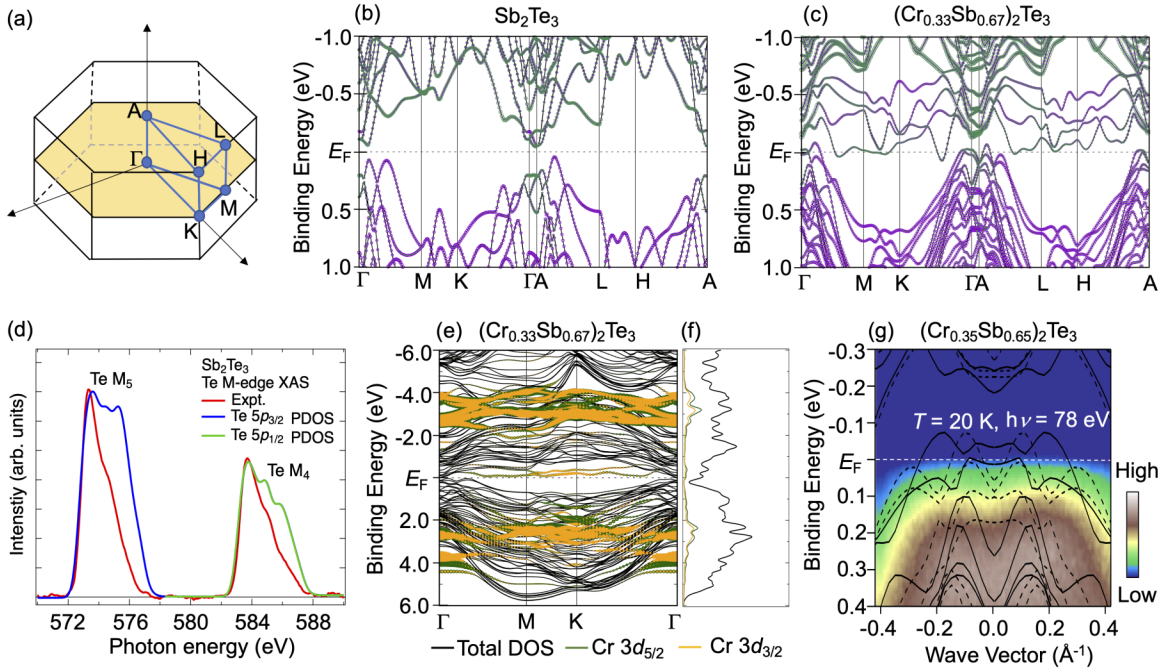

FIG. 4. (a) The Brillouin zone (BZ) of Sb_2Te_3. (a) Calculated band dispersions of Sb_2Te_3 along high-symmetry cuts in the BZ, obtained from LDA band-structure calculations. The Sb (purple) and Te (green) band dispersions (BDs) at and near the Γ-point indicate a gap with band inversion in Sb_2Te_3. (c) Calculated Sb and Te BDs of $(Cr_{0.33}Sb_{0.67})_2Te_3$ obtained from LDA+U band-structure calculations, with $U = 3$ eV. The Sb and Te BDs at and near the Γ-point indicate that a gap just above E_F with band inversion survives with Cr doping. (d) Projected Te $5p_{3/2}$ and $5p_{1/2}$ partial DOS compared with corresponding Te M_5- and M_4-edge XAS spectra. (e) Calculated BDs of $(Cr_{0.33}Sb_{0.67})_2Te_3$ obtained from LDA+U band-structure calculations over a wide energy range. The green and yellow bands are the projected Cr $3d_{5/2}$ and $3d_{3/2}$ bands, and the symbol size represents relative DOS. (f) Corresponding total DOS (black line) and projected Cr $3d_{5/2}$ and $3d_{3/2}$ partial DOS. The Sb-Te p-character bands dominate at and near E_F while the Cr $3d$ states lie at about 2–4 eV below and above E_F. The weak Cr $3d$ states just above E_F in panel (f) mainly come from the M-K cut in the BZ, as seen in panel (e). (g) ARPES intensity map along the Γ-M cut of an *in situ* cleaved surface of $(Cr_{0.35}Sb_{0.65})_2Te_3$ at $T = 20$ K measured with $h\nu = 78$ eV, which probes the bulk valence band. The calculated Sb-Te p-bands along the Γ-M (full lines) and A-L (dashed lines) cuts are overlaid over the experimental map. The states just above E_F at and near the Γ point indicate a small bulk gap of ∼150 meV which can allow TSS formation.

the maximum intensity of the weak bands. The dashed lines were obtained from Figs. 5(c) and 5(d), which show the second derivative of momentum distribution curves (MDCs) of the raw maps shown in Figs. 5(a) and 5(b), indicating that Dirac-type linear bands survive for high Cr doping content at $T = 210$ K in the paramagnetic phase and also at $T = 20$ K in the FM phase. An extrapolation of the band dispersion above E_F suggests that, assuming an absence of changes due to FM ordering, the DP is expected to be at $248 \pm 26/244 \pm 15$ meV at $T = 210$ K/20 K above E_F. The existence of the DP cannot be confirmed by ARPES as it lies far above E_F. However, as we will show in the following, we find spin-sensitive shifts above E_F in $(Cr_{0.35}Sb_{0.65})_2Te_3$ films, but the largest shift is ∼140 meV at $T = 25$ K. This energy is less than the estimated DP at ∼250 meV above E_F, and implies that $(Cr_{0.35}Sb_{0.65})_2Te_3$ is a topologically trivial FM. Also for topological properties like the QAHE to exist, the E_F must lie in a gap, and that is also not satisfied for $(Cr_{0.35}Sb_{0.65})_2Te_3$. This indicates that topological properties cannot survive in $(Cr_{0.35}Sb_{0.65})_2Te_3$.

To check for changes in the leading edges of the Te M-edges and Cr L-edges, in Figs. 6(a)–6(d) we plot the XAS spectra of $(Cr_{0.35}Sb_{0.65})_2Te_3$ with an applied magnetic field of +1 and −1 T for the Te M_5 leading-edge region on an expanded scale (572–573.4 eV) with the same normalization as in Fig. 3. The leading-edge changes indicate a clear and systematic T-dependent energy splitting between +1 and −1 T XAS spectra, due to the redistribution of spin-sensitive spectral weight in XAS and XMCD spectra that occurs below T_C, as shown in Fig. 3(a). Similarly, we plot the T-dependent Cr L_3 leading edge XAS spectra on an expanded scale (573.4–574.2 eV) with applied magnetic fields of +1 and −1 T in Figs. 6(e)–6(h). The spin-sensitive shifts $\gamma_{\text{expt}}(T)$ between the +1 and −1 T at each T are quantified at positions marked by arrows in Figs. 6(a)–6(d) and Figs. 6(e)–6(h), and listed in Table I.

The values of $\gamma_{\text{expt}}(T)$ seen in Figs. 6(a)–6(d) and Figs. 6(e)–6(h) are plotted on the right axis with the sample magnetization and the XMCD intensity on the left axis as a function of T in Fig. 7. The results show that $\gamma_{\text{expt}}(T)$ is proportional to the magnetization and the XMCD intensity as a function of T. Thus, although topological properties are not expected in this material, it still shows T-dependent leading-edge shifts of magnetic origin below the FM ordering temperature. At $T = 25$ K, the Te M_5- and Cr L_3-edge shifts have nearly the same values of 140±10 and 144±10 meV, within error bars. Similarly, we have also plotted the overlapping Te M_4−Cr L_2 leading edge on an expanded scale (∼583.0 to ∼583.5 eV) to check $\gamma_{\text{expt}}(T)$ between +1 and −1 T XAS spectra at each T, as shown in the Appendix,

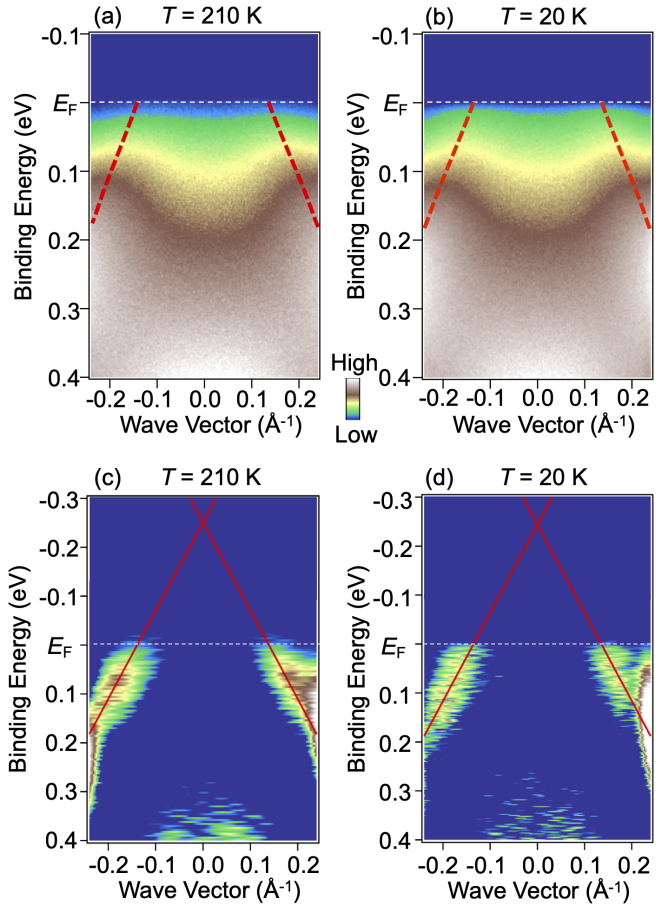

FIG. 5. ARPES intensity maps of *in situ* cleaved surfaces of $(Cr_{0.35}Sb_{0.65})_2Te_3$ films measured at (a) $T = 210$ K and (b) $T = 20$ K. Panels (c) and (d) show the corresponding second derivative maps obtained from the ARPES intensity maps. The observed band dispersions (red dashed lines in (a) and (b)] indicate that the Dirac-type linear dispersions survive at high Cr doping content. Assuming an absence of changes due to FM ordering, a linear extrapolation [red full lines in (c) and (d)] suggests that the DP is expected to be at ∼250 meV above E_F.

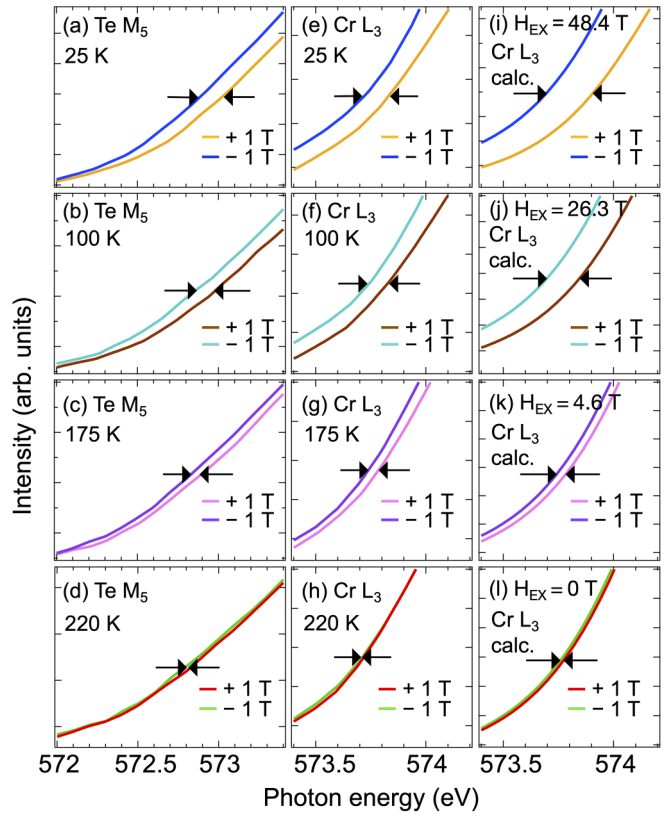

FIG. 6. Spin-sensitive shifts in dopant Cr $3d$ and Te $5p$ states of $(Cr_{0.35}Sb_{0.65})_2Te_3$ ($T_C = 192$ K) with an applied magnetic field of $+1$ and -1 T. (a)–(d) Te M_5-edge and (e)–(h) Cr L_3-edge T-dependent XAS spectra on an expanded scale. The data exhibit systematic spin-sensitive shifts in the Te M_5 and Cr L_3 edges of $(Cr_{0.35}Sb_{0.65})_2Te_3$, with a maximum shift of 140 ± 10 meV and 144 ± 10 meV at $T = 25$ K, respectively. (i)–(l) The corresponding calculated Cr L-edge XAS spectra for different values of exchange field H_{ex} show that the calculated shifts γ_{calc} are proportional to the experimental shifts but are overestimated, with $\gamma_{expt} \sim 0.66 \times \gamma_{calc}$ (see Fig. 7).

Figs. 10(a)–10(d). The overlapping Te M_4−Cr L_2 leading edge also shows a clear spin-sensitive shift between the $+1$ and -1 T XAS spectra (Table II in the Appendix). Another confirmation of the magnetic character of the shift is seen Figs. 10(a)–10(d): since the L_3 (M_5) and L_2 (M_4) levels have opposite spin-orbit coupling, the spin polarization is opposite at the two edges, i.e., the Te M_4−Cr L_2 leading edge shows a clear spin-shift "reversal" compared to the Te M_5 and Cr L_3 leading edges shown in Fig. 6.

The calculations shown in Fig. 3(b) with an exchange field H_{ex}, which quantitatively reproduces the experimental XMCD, also show a spin-sensitive shift γ_{calc} in the Cr XAS L_3 and L_2 leading edges as shown in Figs. 6(i)–6(l) and Figs. 10(e)–10(h), respectively. It is found that the calculations overestimate the shifts, and this is attributed to limitations of a cluster model. A plot of the calculated shift energies γ_{calc} is also included in Fig. 7, and it is proportional to the experimental shifts with $\gamma_{expt} \sim 0.66 \times \gamma_{calc}$. At the lowest $T = 25$ K, the required exchange field H_{ex} of ∼48.4 T corresponds to a Zeeman energy $\zeta = 2.8$ meV $< T_C = 192$ K ($= 16.5$ meV) $\ll \gamma_{expt} \sim 140$ meV. The estimated ζ values are also plotted in Fig. 7 and indicate that the spin-sensitive shifts $\gamma_{expt} \sim 55 \times \zeta$. This suggests the role of Cr $3d$ exchange interactions in causing a relatively large spin-sensitive shift in

TABLE I. The experimental and calculated XMCD %, the experimental Te M_5 and Cr L_3 spin-sensitive shift $\gamma_{expt}(T)$ (error bar is ±10 meV), the calculated Cr L_3 spin-sensitive shift $\gamma_{calc}(T)$, and the exchange field H_{ex}. An applied magnetic field of ± 1 T was used for XMCD experiments and calculations.

T (K)	XMCD expt %	XMCD calc %	Te M_5 γ_{expt} (meV)	Cr L_3 γ_{expt} (meV)	Cr L_3 γ_{calc} (meV)	H_{ex} (T)
25	49.42	49.39	140	144	209.27	48.4
100	35.60	35.54	110	100	149.29	26.3
175	10.09	10.08	33	49	40.62	4.6
220	2.90	3.53	10	5	14.72	0

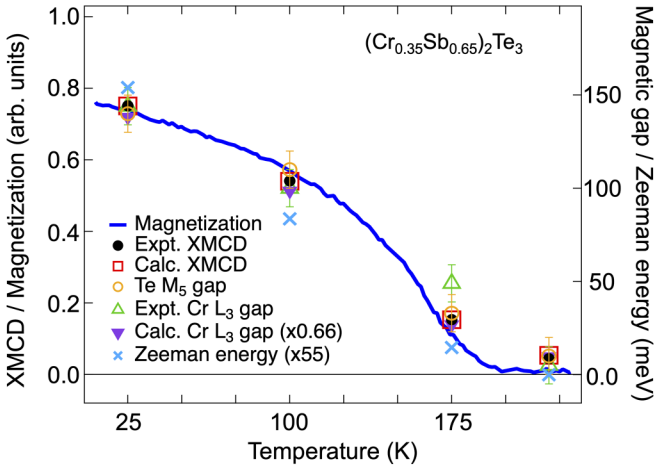

FIG. 7. The XMCD signal and magnetization (left-axis) as a function of T, together with the experimental and calculated spin-sensitive shifts, γ ($\gamma_{\text{expt}} \sim 0.66\gamma_{\text{calc}}$) (right axis). The Zeeman energy ($\times 55$) corresponding to the exchange field is also plotted on the right axis.

Cr $3d$ states, and it induces a comparable spin-sensitive shift via hybridization in Te $5p$ states of $(Cr_{0.35}Sb_{0.65})_2Te_3$.

It is noted that studies on a few FM semiconductors have reported the observation of spin-splitting in conduction-band states, such as EuSe, EuS, EuO (with a spin-splitting of ~180–360 meV), in (In,Fe)As (with a spin-splitting of ~30–50 meV) using spin-polarized tunneling spectroscopy [48–51], and by MCD in optical spectroscopy of nanocrystalline EuSe and EuS [52]. Since the XAS-XMCD measurements were carried out using the total electron yield method, the electron sampling depth at the Cr L-edge/Te M-edge energies is ~15–20 Å [53]. Thus, the technique is considered to be less surface-sensitive than ARPES measurements shown in Figs. 4 and 5, as well as spin-polarized tunneling spectroscopy [48–51].

In Fig. 8, using the known occupied Cr $3d$ states reported by resonant-PES [25,47] and our XAS and ARPES results, we show a schematic of the electronic structure of Cr $3d$ and Te $5p$ states of $(Cr_{0.35}Sb_{0.65})_2Te_3$. Resonant-PES showed that the Cr^{3+} $t_{2g\uparrow}$ states lie ~2 eV below E_F [25,47], and cluster model calculations indicate a negative $\Delta = -2.0$ eV, $U_{dd} = 4.0$ eV, and strong $V_{eg} = 1.35$ eV (Ref. [24] and the present work). Hence, the lowest unoccupied states have Te $5p$ character, consistent with a band inversion. Accordingly, the unoccupied Cr^{3+} $t_{2g\downarrow}$ states and the Cr^{3+} $e_{g\uparrow}$ states lie above the Te $5p$ unoccupied states. Based on $\pm$1T applied field and exchange field-dependent spectral shape changes at low-T, the FM transition manifests as a spin-sensitive leading-edge shift, which we interpret as due to spin-splitting between lowest energy unoccupied Cr^{3+} $t_{2g\downarrow}$ states and the Cr^{3+} $e_{g\uparrow}$ states (Fig. 8), and it induces a spin-sensitive shift in the unoccupied Te $5p$ states above E_F. Our results indicate $(Cr_{0.35}Sb_{0.65})_2Te_3$ has nearly all the features of the very recently predicted route to QAHE [54], namely a strongly correlated half-filled band, an "inverted" or negative Δ, and band inversion. However, since the largest γ_{expt} value of ~140 meV observed at $T = 25$ K is less than the estimated DP at ~250 meV above E_F, and furthermore since the material is metallic and the E_F does not lie in a gap, the topological properties cannot survive in $(Cr_{0.35}Sb_{0.65})_2Te_3$.

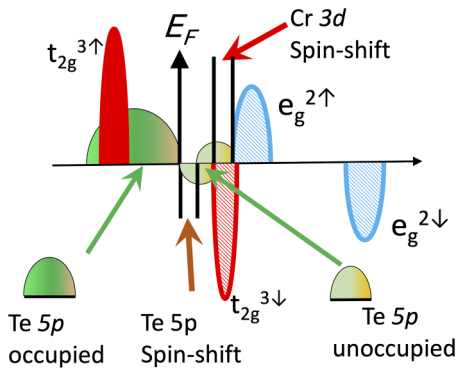

FIG. 8. Schematic of the electronic structure of the negative charge-transfer ($\Delta < 0$) system $(Cr_{0.35}Sb_{0.65})_2Te_3$ inferred from the experiments and calculations, showing the Cr $3d$ and Te $5p$ band assignments and the spin-sensitive shift, which we interpret as due to spin-splitting. The color gradation in Te $5p$ states is used to indicate hybridization with Sb $5p$ and Cr $3d$ states and represents band inversion and a negative charge-transfer energy.

IV. CONCLUSIONS

In conclusion, our study on $(Cr_{0.35}Sb_{0.65})_2Te_3$ shows that the T-dependent XAS-XMCD exhibit spin-sensitive shifts in the electronic structure which follows the bulk magnetization, XMCD intensity, and the exchange field. ARPES measurements showed linear bands, but the estimated DP energy is larger than γ_{expt} ($T = 25$ K), implying a topologically trivial FM. The Cr $3d$ XMCD spectra can be described by charge-transfer multiplet cluster model calculations with a negative charge-transfer energy Δ between Cr $3d$ and Te $5p$ states. The study establishes a direct link between unoccupied Cr $3d$ dopant and Te $5p$ spin-sensitive states in $(Cr_{0.35}Sb_{0.65})_2Te_3$ with the magnetization, XMCD intensity, and exchange field. Since the T-dependent spin-sensitive shifts γ_{expt} in the Cr $3d$ states can be simulated by a relatively low exchange field, it suggests the role of Cr $3d$ exchange interactions in enhancing the spin-sensitive shifts in Cr $3d$ states, and induces comparable spin-sensitive shifts via hybridization in Te $5p$ states of $(Cr_{0.35}Sb_{0.65})_2Te_3$.

ACKNOWLEDGMENTS

C.W.C. and Y.N. and acknowledge support from JSPS and GP-Spin at Tohoku University. T.S. thanks JST-CREST (No. JP-MJCR18T1) for financially supporting this research. This work was supported by JSPS KAKENHI (Grant No. funding JP-22K03535). A.F. acknowledges support from the Yushan Fellow Program under the Ministry of Education of Taiwan. A.C. thanks the National Science and Technology Council (NSTC), Taiwan, Republic of China, for financially supporting this research under Contract No. NSTC 111-2112-M-213-031.

APPENDIX

1. XAS data analysis

Figure 9 shows the raw Cr L-edge and Te M-edge XAS spectra obtained from *in situ* cleaved surfaces of $(Cr_{0.35}Sb_{0.65})_2Te_3$ measured at (a) $T = 220$ K and (b) $T = 25$ K with an applied magnetic field of $\pm$ 1 T. It is seen that the XAS spectra show a large background, but the background is very similar for both $+1$ and -1 T spectra. To compare the experimental XAS with calculated XAS spectra, a polynomial background as shown in Fig. 9 was subtracted from the raw data to obtain the XAS spectra shown in Fig. 3(a) of the main paper.

2. Cluster model calculations

We carried out charge-transfer multiplet cluster model calculations for the Cr $2p$-$3d$ XAS based on a Cr L_6 (L = ligand) cluster using the QUANTY program [35–37]. We used an octahedral O_h symmetry cluster with a formal valency of trivalent Cr ion and four basis states given by $d^{n+p}L^p$ states ($n = 3$ and p = 0–3), following the recent study by Tcakaev *et al.* [24]. As usual, the electronic parameters of the calculation are the charge-transfer (CT) energy Δ, which is defined as the energy separation between the d^n state and the $d^{n+1}\underline{L}$ state, the on-site Coulomb energy U_{dd}, the core-hole potential or the Coulomb interaction energy between Cr $2p$ core hole and

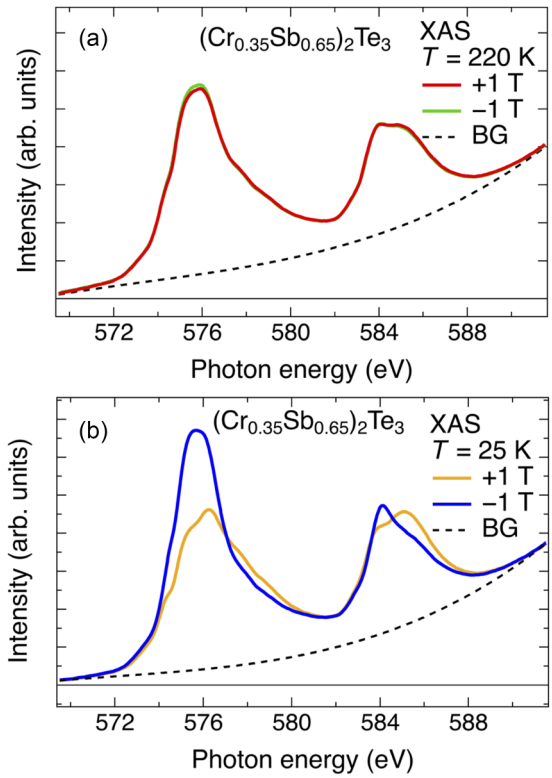

FIG. 9. The raw Cr L-edge and Te M-edge XAS spectra from *in situ* cleaved surfaces of $(Cr_{0.35}Sb_{0.65})_2Te_3$ measured at (a) $T = 220$ K and (b) $T = 25$ K with an applied magnetic field of $\pm$ 1 T. The dashed curve indicates the polynomial background subtracted from the data to obtain the spectra shown in Fig. 3 of the main paper.

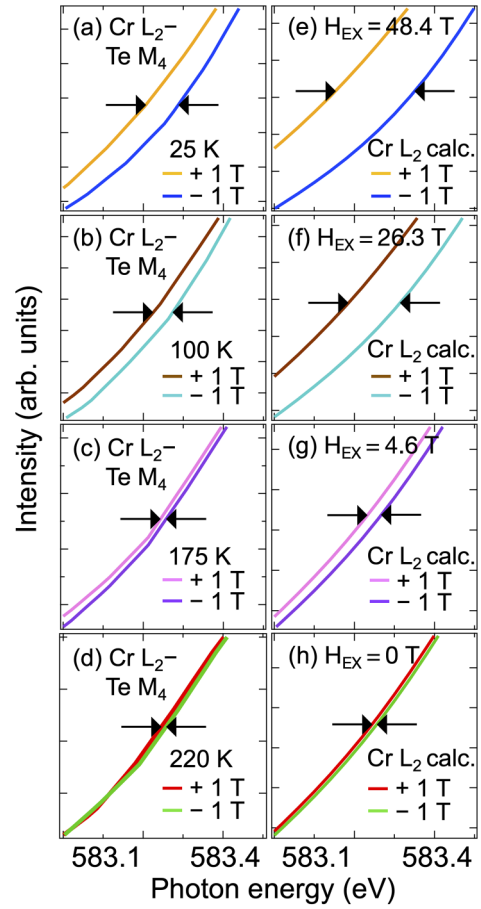

FIG. 10. The expanded scale Te M_4-Cr L_2-edge T-dependent XAS experimental (a)–(d) and calculated (e)–(h) spectra showing a spin-shift reversal as the leading edges show a clear switching for an applied magnetic field of $+1$ and -1 T compared to the Te M_5- and Cr L_3-edge results shown in Fig. 3.

$3d$ electrons U_{cd}, the hybridization energies V_{e_g} and $V_{t_{2g}}$, and the crystal-field splitting $10Dq$, which is the energy splitting between the t_{2g} and e_g states. The spin-orbit coupling is also included in the calculations. A suitable match was obtained for the electronic parameter values of on-site Coulomb energy $U_{dd} = 4.0$ eV, core-hole potential $U_{cd} = 4.8$ eV, hybridization strengths $V_{e_g} = 1.35$ eV, $V_{t_{2g}} = 0.5$ eV, crystal-field splitting $10Dq = 1.0$ eV, and $\Delta = -2.0$ eV. Most importantly, we also needed to consider the internal

TABLE II. The experimental Cr L_2-Te M_4 and calculated Cr L_2 spin-sensitive shifts, γ_{expt} and γ_{calc}, with an error bar of $\pm$10 meV, and the exchange field H_{ex}.

	Cr L_2/Te M_4	Cr L_2	
T (K)	γ_{expt} (meV)	γ_{calc} (meV)	H_{ex} (T)
25	81.34	196.66	48.4
100	48.82	128.87	26.3
175	14.06	34.01	4.6
220	11.96	11.96	0

exchange field H_{ex} in order to obtain the XMCD intensity variation and the spin-sensitive shifts in the leading edges as a function of T seen in the experiments.

3. Spin-sensitive shifts in the M_4-L_2-edge of $(Cr_{0.35}Sb_{0.65})_2Te_3$

The overlapping Te M_4 − Cr L_2 edge is plotted in Figs. 10(a)–10(d) on an expanded scale (∼583.0 to ∼583.5 eV) for comparing the spin-sensitive shifts between +1 and −1 T XAS spectra. The Te M_4 − Cr L_2 leading edge shows a clear spin-sensitive shift γ_{expt} and the values are listed in Table II. As seen in Figs. 10(a)–10(d), the spin polarization is opposite at the L_2-M_4 edge compared to the L_3 and M_5 edges [Figs. 6(a)–6(h)], because the L_3 (M_5) and L_2 (M_4) levels have opposite spin-orbit coupling. This indicates that the Te M_4 − Cr L_2 leading edge shows a clear spin-shift "reversal" compared to the Te M_5 and Cr L_3 leading edges shown in Fig. 6. This spin-sensitive shift reversal is also confirmed in the calculated spectra, although it is overestimated, as shown in Figs. 10(e)–10(h), and the corresponding values are listed in Table II.

[1] C. L. Kane and E. J. Mele, Z_2 topological order and the quantum spin Hall effect, Phys. Rev. Lett. **95**, 146802 (2005).

[2] L. Fu and C. L. Kane, Topological insulators with inversion symmetry, Phys. Rev. B **76**, 045302 (2007).

[3] L. Fu, C. L. Kane, and E. J. Mele, Topological insulators in three dimensions, Phys. Rev. Lett. **98**, 106803 (2007).

[4] R. Yu *et al.*, Quantized anomalous Hall effect in magnetic topological insulators, Science **329**, 61 (2010).

[5] K. Nomura and N. Nagaosa, Surface-quantized anomalous Hall current and the magnetoelectric effect in magnetically disordered topological insulators, Phys. Rev. Lett. **106**, 166802 (2011).

[6] C.-Z. Chang *et al.*, Experimental observation of the quantum anomalous Hall effect in a magnetic topological insulator, Science **340**, 167 (2013).

[7] Y. Ando, Topological Insulator materials, J. Phys. Soc. Jpn. **82**, 102001 (2013).

[8] Y. Tokura, K. Yasuda, and A. Tsukazaki, Magnetic topological insulators, Nat. Rev. Phys. **1**, 126 (2019).

[9] Y. L. Chen *et al.*, Massive Dirac fermion on the surface of a magnetically doped topological insulator, Science **329**, 659 (2010).

[10] S.-Y. Xu *et al.*, Hedgehog spin texture and Berry's phase tuning in a magnetic topological insulator, Nat. Phys. **8**, 616 (2012).

[11] D. Zhang *et al.*, Interplay between ferromagnetism, surface states, and quantum corrections in a magnetically doped topological insulator, Phys. Rev. B **86**, 205127 (2012).

[12] J. Sanchez-Barriga *et al.*, Nonmagnetic band gap at the Dirac point of the magnetic topological insulator $(Bi_{1-x}Mn_x)_2Se_3$, Nat. Commun. **7**, 10559 (2016).

[13] I. Lee *et al.*, Imaging Dirac-mass disorder from magnetic dopant atoms in the ferromagnetic TI $Cr_x(Bi_{0.1}Sb_{0.9})_2Te_3$, Proc. Natl. Acad. Sci. USA **112**, 1316 (2015).

[14] C.-Z. Chang *et al.*, Chemical-potential-dependent gap opening at the Dirac surface states of Bi_2Se_3 induced by aggregated substitutional Cr atoms, Phys. Rev. Lett. **112**, 056801 (2014).

[15] E. D. L. Rienks *et al.*, Large magnetic gap at the Dirac point in $Bi_2Te_3/MnBi_2Te_4$ heterostructures, Nature (London) **576**, 423 (2019).

[16] R. Lu, H. Sun, S. Kumar, Y. Wang, M. Gu, M. Zeng, Y. J. Hao, J. Li, J. Shao, X. M. Ma, Z. Hao, K. Zhang, W. Mansuer, J. Mei, Y. Zhao, C. Liu, K. Deng, W. Huang, B. Shen, K. Shimada, E. F. Schwier, C. Liu, Q. Liu, and C. Chen, Half-magnetic topological insulator with magnetization-induced Dirac gap at a selected surface, Phys. Rev. X **11**, 011039 (2021); Erratum: Half-magnetic topological insulator with magnetization-induced Dirac gap at a selected surface [Phys. Rev. X 11, 011039 (2021)], **11**, 029902(E) (2021).

[17] S. Wimmer, J. Snchez-Barriga, P. Kppers, A. Ney, E. Schierle, F. Freyse, O. Caha, J. Michalicka, M. Liebmann, D. Primetzhofer, M. Hoffman, A. Ernst, M. M. Otrokov, G. Bihlmayer, E. Weschke, B. Lake, E. V. Chulkov, M. Morgenstern, G. Bauer, G. Springholz, and O. Rader, Mn-Rich $MnSb_2Te_4$: A topological insulator with magnetic gap closing at high Curie temperatures of 45–50 K, Adv. Mater. **33**, 2102935 (2021).

[18] K. Sumida *et al.*, Ultrafast surface Dirac fermion dynamics of Sb_2Te_3-based topological insulators, Prog. Surf. Sci. **96**, 100628 (2021).

[19] M. Ye *et al.*, Carrier-mediated ferromagnetism in the magnetic topological insulator Cr-doped $(Sb, Bi)_2Te_3$, Nat. Commun. **6**, 8913 (2015)

[20] K. Hori, S. Souma, C.-W. Chuang, Y. Nakata, K. Nakayama, S. Gupta, T. P. T. Nguyen, K. Yamauchi, T. Takahashi, F. Matsukura, F. H. Chang, H. J. Lin, C. T. Chen, A. Chainani, and T. Sato, Unusual band evolution and persistence of topological surface states in high-T_C magnetic topological insulator, arXiv:2307.13388.

[21] J. S. Dyck, P. Hájek, P. Lošták, and C. Uher, Diluted magnetic semiconductors based on $Sb_{2-x}V_xTe_3$ ($\sim 0.01 < x < \sim 0.03$), Phys. Rev. B **65**, 115212 (2002); J. S. Dyck, Č. Drastar, P. Lošták, and C. Uher, Low-temperature ferromagnetic properties of the diluted magnetic semiconductor $Sb_{2-x}Cr_xTe_3$, *ibid.* **71**, 115214 (2005).

[22] Z. Zhou, Y.-J. Chien, and C. Uher, Thin film dilute ferromagnetic semiconductors $Sb_{2-x}Cr_xTe_3$ with a Curie temperature up to 190 K, Phys. Rev. B **74**, 224418 (2006).

[23] L. B. Duffy, A. I. Figueroa, Ł. Gadczuk, N.-J. Steinke, K. Kummer, G. van der Laan, and T. Hesjedal, Magnetic proximity coupling to Cr-doped Sb_2Te_3 thin films, Phys. Rev. B **95**, 224422 (2017).

[24] A. Tcakaev, V. B. Zabolotnyy, R. J. Green, T. R. F. Peixoto, F. Stier, M. Dettbarn, S. Schreyeck, M. Winnerlein, R. C. Vidal, S. Schatz *et al.*, Comparing magnetic ground-state properties of the V- and Cr-doped TI $(Bi, Sb)_2Te_3$, Phys. Rev. B **101**, 045127 (2020).

[25] T. R. F. Peixoto *et al.*, Non-local effect of impurity states on the exchange coupling mechanism in magnetic topological insulators, npj Quantum Mater. **5**, 87 (2020).

[26] J. Henk, M. Flieger, I. V. Maznichenko, I. Mertig, A. Ernst, S. V. Eremeev, and E. V. Chulkov, Topological character and

magnetism of the Dirac state in Mn-doped Bi_2Te_3, Phys. Rev. Lett. **109**, 076801 (2012).

[27] F. M. F. de Groot, X-ray absorption and dichroism of transition metals and their compounds, J. Electron Spectrosc. Relat. Phenom. **67**, 529 (1994).

[28] J. Stohr and H. C. Siegmann, *Magnetism From Fundamentals to Nanoscale Dynamics* (Springer-Verlag, Berlin, 2006).

[29] S. Gupta, S. Kanai, F. Matsukura, and H. Ohno, Magnetic and transport properties of Sb_2Te_3 doped with high concentration of Cr, Appl. Phys. Express **10**, 103001 (2017).

[30] I. Rajput, S. Rana, R. P. Jena, and A. Lakhani, Crystal growth and x-ray diffraction characterization of Sb_2Te_3 single crystal, *AIP Conf. Proc. No. 2100*, edited by N. Kaurav, K. K. Choudhary, R. C. Dixit, and A. Mishra (AIP, New York, 2019), p. 020070.

[31] C. Pauly, G. Bihlmayer, M. Liebmann, M. Grob, A. Georgi, D. Subramaniam, M. R. Scholz, J. Sanchez-Barriga, A. Varykhalov, S. Blugel, O. Rader, and M. Morgenstern, Probing two topological surface bands of Sb_2Te_3 by spin-polarized photoemission spectroscopy, Phys. Rev. B **86**, 235106 (2012).

[32] S. Souma, T. Sato, T. Takahashi, and P. Baltzer, High-intensity xenon plasma discharge lamp for bulk-sensitive high-resolution photoemission spectroscopy, Rev. Sci. Instrum. **78**, 123104 (2007).

[33] J. F. Moulder, W. F. Stickle, P. E. Sobol, and K. D. Bomben, *Handbook of X-ray Photoelectron Spectroscopy* (Physical Electronics, Eden Prairie, MN, 1995).

[34] V. V. Krishnamurthy, D. J. Keavney, D. Haskel, J. C. Lang, G. Srajer, B. C. Sales, D. G. Mandrus, and J. L. Robertson, Temperature dependence of Eu 4f and Eu 5d magnetizations in the filled skutterudite $EuFe_4Sb_{12}$, Phys. Rev. B **79**, 014426 (2009).

[35] M. W. Haverkort, M. Zwierzycki, and O. K. Andersen, Multiplet ligand-field theory using Wannier orbitals, Phys. Rev. B **85**, 165113 (2012).

[36] Y. Lu, M. Hoppner, O. Gunnarsson, and M. W. Haverkort, Efficient real-frequency solver for dynamical mean-field theory, Phys. Rev. B **90**, 085102 (2014).

[37] M. Haverkort, G. Sangiovanni, P. Hansmann, A. Toschi, Y. Lu, and S. Macke, Bands, resonances, edge singularities and excitons in core level spectroscopy investigated within the dynamical mean-field theory, Europhys. Lett. **108**, 57004 (2014).

[38] J. Kim, S.-H. Jhi, A. H. MacDonald, and R. Wu, Ordering mechanism and quantum anomalous Hall effect of magnetically doped topological insulators, Phys. Rev. B **96**, 140410(R) (2017).

[39] Y. Ruan *et al.*, Band-structure engineering of the magnetically Cr-doped topological insulator Sb_2Te_3 under mechanical strain, J. Phys.: Condens. Matter **31**, 385501 (2019).

[40] D. M. Burn, L. B. Duffy, R. Fujita, S. L. Zhang, A. I. Figueroa, J. Herrero-Martin, G. van der Laan, and T. Hesjedal, Cr_2Te_3 thin films for integration in magnetic topological insulator heterostructures, Sci. Rep. **9**10793 (2019).

[41] T. Mizokawa, H. Namatame, A. Fujimori, K. Akeyama, H. Kondoh, H. Kuroda, and N. Kosugi, Origin of the band gap in the negative charge-transfer-energy compound $NaCuO_2$, Phys. Rev. Lett. **67**, 1638 (1991).

[42] S. Nimkar, D. D. Sarma, and H. R. Krishnamurthy, Electronic structure of $NaCuO_2$, Phys. Rev. B **47**, 10927 (1993).

[43] V. Bisogni, S. Catalano, R. J. Green, M. Gibert, R. Scherwitzl, Y. Huang, V. N. Strocov, P. Zubko, S. Balandeh, J.-M. Triscone, G. Sawatzky, and T. Schmitt, Ground-state oxygen holes and the metal-insulator transition in the negative charge-transfer rare-earth nickelates, Nat. Commun. **7**, 13017 (2016).

[44] M. Grioni, J. F. van Acker, M. T. Czyzyk, and J. C. Fuggle, Unoccupied electronic structure and core-hole effects in the x-ray-absorption spectra of Cu_2O, Phys. Rev. B **45**, 3309 (1992).

[45] J. R. Vegelius, K. O. Kvashnina, H. Hollmark, M. Klintenberg, Y. O. Kvashnin, I. L. Soroka, L. Werme, and S. M. Butorin, X-ray spectroscopic study of Cu_2S, CuS, and copper films exposed to Na_2S solutions, J. Phys. Chem. C **116**, 22293 (2012).

[46] T. P. T. Nguyen, K. Yamauchi, T. Oguchi, D. Amoroso, and S. Picozzi, Electric-field tuning of the magnetic properties of bilayer VI_3: A first-principles study, Phys. Rev. B **104**, 014414 (2021).

[47] M. F. Islam, C. M. Canali, A. Pertsova, A. Balatsky, S. K. Mahatha, C. Carbone, A. Barla, K. A. Kokh, O. E. Tereshchenko, E. Jimenez *et al.*, Systematics of electronic and magnetic properties in the transition metal doped Sb_2Te_3 quantum anomalous Hall platform, Phys. Rev. B **97**, 155429 (2018).

[48] L. Esaki, P. J. Stiles, and S. von Molnar, Magnetointernal field emission in junctions of magnetic insulators, Phys. Rev. Lett. **19**, 852 (1967).

[49] J. S. Moodera, X. Hao, G. A. Gibson, and R. Meservey, Electron-spin polarization in tunnel junctions in zero applied field with ferromagnetic EuS barriers, Phys. Rev. Lett. **61**, 637 (1988).

[50] T. S. Santos, J. S. Moodera, K. V. Raman, E. Negusse, J. Holroyd, J. Dvorak, M. Liberati, Y. U. Idzerda, and E. Arenholz, Determining exchange splitting in a magnetic semiconductor by spin-filter tunneling, Phys. Rev. Lett. **101**, 147201 (2008).

[51] L. D. Anh, P. N. Hai, and M. Tanaka, Observation of spontaneous spin-splitting in the band structure of an n-type zinc-blende ferromagnetic semiconductor, Nat. Commun. **7**, 13810 (2016).

[52] D. R. C. Asuigui, D. James, D. R. Gamelin, M. C. De Siena, and S. L. Stoll, Giant band splittings in EuS and EuSe magnetic semiconductor nanocrystals, Chem. Commun. **56**, 5843 (2020).

[53] R. Nakajima, J. Stohr, and Y. U. Idzerda, Electron-yield saturation effects in L-edge x-ray magnetic circular dichroism spectra of Fe, Co, and Ni, Phys. Rev. B **59**, 6421 (1999).

[54] T. Devakul and L. Fu, Quantum anomalous Hall effect from inverted charge transfer gap, Phys. Rev. X **12**, 021031 (2022).